energies

MDPI

Article

Front Movement and Sweeping Rules of CO_2 Flooding under Different Oil Displacement Patterns

Xiang Qi [1,2], Tiyao Zhou [1,2], Weifeng Lyu [1,2,*], Dongbo He [1,2,3,*], Yingying Sun [1,2], Meng Du [1,2], Mingyuan Wang [1,2] and Zheng Li [1,2]

[1] PetroChina Research Institute of Petroleum Exploration & Development, Beijing 100083, China; qixiang@petrochina.com.cn (X.Q.); zhoutiyao@petrochina.com.cn (T.Z.); sunyingying@petrochina.com.cn (Y.S.); dumeng22@petrochina.com.cn (M.D.); wangmy21@petrochina.com.cn (M.W.); lizheng21@petrochina.com.cn (Z.L.)
[2] State Key Laboratory of Enhanced Oil and Gas Recovery, Beijing 100083, China
[3] JiDong Oilfield of PetroChina, Tangshan 063200, China
* Correspondence: lweifeng@petrochina.com.cn (W.L.); 311@petrochina.com.cn (D.H.)

Abstract: CO_2 flooding is a pivotal technique for significantly enhancing oil recovery in low-permeability reservoirs. The movement and sweeping rules at the front of CO_2 flooding play a critical role in oil recovery; yet, a comprehensive quantitative analysis remains an area in need of refinement. In this study, we developed 1-D and 2-D numerical simulation models to explore the sweeping behavior of miscible, immiscible, and partly miscible CO_2 flooding patterns. The front position and movement rules of the three CO_2 flooding patterns were determined. A novel approach to the contour area calculation method was introduced to quantitatively characterize the sweep coefficients, and the sweeping rules are discussed regarding the geological parameters, oil viscosity, and injection–production parameters. Furthermore, the Random Forest (RF) algorithm was employed to identify the controlling factor of the sweep coefficient, as determined through the use of out-of-bag (OOB) data permutation analysis. The results showed that the miscible front was located at the point of maximum CO_2 content in the oil phase. The immiscible front occurred at the point of maximum interfacial tension near the production well. Remarkably, the immiscible front moved at a faster rate compared with the miscible front. Geological parameters, including porosity, permeability, and reservoir thickness, significantly impacted the gravity segregation effect, thereby influencing the CO_2 sweep coefficient. Immiscible flooding exhibited the highest degree of gravity segregation, with a maximum gravity segregation degree (GSD) reaching 78.1. The permeability ratio was a crucial factor, with a lower limit of approximately 5.0 for reservoirs suitable for CO_2 flooding. Injection–production parameters also played a pivotal role in terms of the sweep coefficient. Decreased well spacing and increased gas injection rates were found to enhance sweep coefficients by suppressing gravity segregation. Additionally, higher gas injection rates could improve the miscibility degree of partly miscible flooding from 0.69 to 1.0. Oil viscosity proved to be a significant factor influencing the sweep coefficients, with high seepage resistance due to increasing oil viscosity dominating the miscible and partly miscible flooding patterns. Conversely, gravity segregation primarily governed the sweep coefficient in immiscible flooding. In terms of controlling factors, the permeability ratio emerged as a paramount influence, with a factor importance value (FI) reaching 1.04. The findings of this study can help for a better understanding of sweeping rules of CO_2 flooding and providing valuable insights for optimizing oil recovery strategies in the field applications of CO_2 flooding.

Keywords: CO_2 front; sweep coefficient; Random Forest; main controlling factor

check for updates

Citation: Qi, X.; Zhou, T.; Lyu, W.; He, D.; Sun, Y.; Du, M.; Wang, M.; Li, Z. Front Movement and Sweeping Rules of CO_2 Flooding under Different Oil Displacement Patterns. *Energies* **2024**, *17*, 15. https://doi.org/10.3390/en17010015

Academic Editor: Riyaz Kharrat

Received: 25 October 2023
Revised: 5 December 2023
Accepted: 14 December 2023
Published: 19 December 2023

Copyright: © 2023 by the authors. Licensee MDPI, Basel, Switzerland. This article is an open access article distributed under the terms and conditions of the Creative Commons Attribution (CC BY) license (https://creativecommons.org/licenses/by/4.0/).

1. Introduction

The escalating emissions of greenhouse gases, predominantly carbon dioxide (CO_2), have led to a myriad of environmental challenges, including global climate change [1].

Statistics reveal that a staggering 64% of environmental pollution originates from the increasing concentration of CO_2 in the atmosphere [2]. In response to these concerns, China has aimed to peak carbon emissions by 2030 and achieve carbon neutrality by 2060 [3]. Carbon capture, utilization, and storage (CCUS) have emerged as pivotal strategies in addressing the global climate crisis. This technology involves the capture and separation of CO_2 from industrial emissions, followed by its beneficial utilization, ultimately contributing to a reduction in overall CO_2 emissions [4]. CCUS represents a win–win solution, fostering resource utilization and effective emission reduction. Particularly in the field of petroleum engineering, the application of CO_2 flooding holds promising prospects in terms of significantly enhancing oil recovery in low-permeability reservoirs [5].

As reservoir exploration continues, the proportion of conventional medium and high-permeability reservoir reserves is gradually decreasing, while the discovery of low-permeability reservoir reserves is steadily increasing [6–9]. In comparison with water flooding, carbon dioxide (CO_2) possesses lower density and viscosity, enabling it to penetrate even the tiny pores, improving the micro-sweep coefficient [10–12]. When the pressure exceeds the minimum miscible pressure (MMP), CO_2 can eliminate the interfacial tension between oil and gas through multi-contact miscibility, thus significantly enhancing the oil displacement efficiency [13–17]. Consequently, CO_2 flooding holds promising prospects for effectively enhancing oil recovery in low-permeability reservoirs. In addition, CO_2 can also enhance oil recovery by promoting crude oil expansion, reducing crude oil density and viscosity, changing reservoir wettability, and increasing reservoir permeability [18–21]. According to statistics, the application of CCUS technology in low-permeability oil fields in China's Daqing and Jilin regions can enhance oil recovery rates by 10–25% [22]. In the United States, the Kelly–Snyder oil field in the Permian Basin implemented a CO_2 miscible flooding project in the SACROC block in 2002, resulting in a cumulative increase of 2456×10^4 tons of crude oil and an estimated recovery rate improvement of over 26% [23].

The oil recovery within a reservoir is a product of both the sweep coefficient and the displacement efficiency [24]. In the case of miscible CO_2 flooding, the theoretical oil displacement efficiency can attain a remarkable 100%. Therefore, precise quantitative characterization of the CO_2 sweep coefficient holds immense importance in evaluating the enhanced oil recovery potential of CO_2 flooding. Furthermore, in low-permeability reservoirs, the challenges of severe heterogeneity, gravity segregation, and viscous fingering can lead to issues such as gas channeling and a low sweep coefficient [25,26]. To address these challenges effectively, conformance control technologies like WAG flooding and foam flooding become necessary [27–29]. A quantitative analysis of the sweep coefficient serves as the foundational basis for evaluating the efficacy of these conformance control technologies.

Characterizing the sweep coefficient involves both experimental and numerical simulation approaches [30–33]. Concerning experimental simulation, Bergit et al. [34] used high-resolution micro-positron emission tomography (μPET) to analyze the distribution of CO_2 in the core with the change of the PV number during CO_2 injection, and the sweeping effect was characterized qualitatively. Wang et al. [35] used a high-resolution nuclear magnetic resonance method and normalized MI value to distinguish the sweeping range of CO_2 in the core and studied the sweep characteristics of miscible and immiscible flooding. The results showed that the CO_2 front of immiscible flooding is more unstable, which affects the sweep coefficient of CO_2 flooding. Duraid et al. [36] used X-ray CT imaging technology to identify the distribution of oil and water in the heterogeneous core after CO_2 flooding. The results showed that the proportion of residual oil in the low-permeability part is significantly higher than that in the high-permeability part, which indirectly characterized the sweeping rules of CO_2 flooding. The visualization experiment can reflect the microscopic sweep characteristics of CO_2 flooding, and the core experiment can reflect the effect of CO_2 flooding from the macroscopy, but the numerical simulation method is helpful to analyze the sweep rules in detail. Lewis et al. [37] established a reservoir numerical model of a one-quarter five-point well pattern to study water, gas, and WAG flooding sweep

coefficients. The sweep coefficients were calculated assuming that the oil displacement efficiency of gas flooding was 100%. Hao et al. [38] established a numerical simulation model of miscible flooding, delineating the contour line with oil and gas interfacial tension equal to 0.1 dyn/cm as the rear edge of the miscible zone and taking the CO_2 content in the oil phase equal to 20% as the front edge of the miscible zone, thus obtaining the sweep coefficient of CO_2 miscible flooding. Li et al. [39] established a mathematical model of miscible flooding considering CO_2 diffusion and adsorption and defined the location where a dimensionless CO_2 concentration of $C/C_0 = 0.5$ serves as the miscible front and the place where $C/C_0 = 0.95$ serves as the gas phase front to study the migration rule of the CO_2. C is the concentration of CO_2, and C_0 is the initial concentration of CO_2, which is 0.6 $g{\cdot}cm^{-3}$. When the adsorption is weak, increased porosity and initial injection rate accelerate the mass transfer and diffusion process. The stronger the diffusion effect, the larger the miscible region and the earlier the gas breakthrough. Enhanced adsorption reduces the sweeping range of the miscible zone. Li et al. [40] established a numerical simulation model of CO_2 flooding with a five-spot well pattern and an inverted nine-spot well pattern and proposed that the location where the viscosity of crude oil drops to a certain extent is defined as the miscible front, thus studying the CO_2 flooding sweeping rules of different well patterns. The results showed that the sweep coefficient of the inverted nine-spot well pattern was higher than that of the five-spot well pattern.

The factors affecting the CO_2 sweep coefficient include geological factors, fluid properties, the injection–production relationship, and so on [24,41,42]. Analyzing the main controlling factors affecting the CO_2 sweep coefficient is propitious when choosing suitable conformance control technology to improve the application effect of CO_2 flooding. Limited research has delved into identifying the main controlling factor in terms of the CO_2 sweep coefficient, with prevalent methodologies encompassing fuzzy analysis and orthogonal analysis [43,44]. Li et al. [45] evaluated the influence degrees of multiple factors on gas channeling through fuzzy analysis and concluded that fractures and heterogeneity are the most critical factors affecting gas channeling. Cui et al. [46] used orthogonal analysis to establish that the main controlling factor affecting the CO_2 sweep coefficient is well distance and established the calculation formula of the CO_2 sweep coefficient using multiple nonlinear regression methods. However, it is important to note that the selection of the weight matrix in fuzzy analysis is somewhat subjective, potentially impacting the precision of the main controlling factor analysis. Moreover, the limited data samples employed in orthogonal studies can lead to specific errors when analyzing the primary controlling factors. Consequently, there exists a need for the further exploration of methodologies for analyzing the main controlling factor influencing the CO_2 flooding sweep coefficient.

According to the relationship between reservoir pressure and minimum miscible pressure (MMP), CO_2 flooding is traditionally categorized into miscible flooding (MF) and immiscible flooding (IMF). However, throughout the reservoir development process, the continuous injection of CO_2 induces dynamic changes in the reservoir pressure distribution, leading to alterations in the miscible state of CO_2 and crude oil. Based on the pressure distribution between injection and production wells, we proposed a more nuanced classification of CO_2 flooding into three distinct displacement patterns: miscible flooding (MF), partly miscible flooding (IMF), and immiscible flooding (IMF). The position and migration law of the miscible front and the immiscible front under three displacement patterns were studied. The quantitative characterization of the sweep coefficients across these patterns was achieved through the application of the contour area method. Additionally, we elucidated the impact of geological factors, injection–production parameters, and crude oil viscosity on the sweep coefficients. Utilizing the Random Forest algorithm, we identified the main controlling factor influencing the sweep coefficient in CO_2 flooding. The findings of this study can help for providing valuable insights for optimizing oil recovery strategies in the field applications of CO_2 flooding. Sections 4.1 and 4.2 are dedicated to the fitting of PVT (pressure–volume–temperature) and slim tube experiment results carried out in the Jilin low-permeability oil field. Based on the fitting results, 1-D and 2-D numerical simulation

models of CO_2 flooding were developed. Section 4.3 focuses on pinpointing the locations of both miscible and immiscible fronts through an analysis of the fluid property variations between wells within the 1-D model. In Section 4.4, based on the contour area method, the CO_2 sweep coefficients for different flooding patterns within the 2-D model are calculated using MATLAB software. Furthermore, we introduce parameters such as GSD (gravity segregation degree) and D_m (miscible degree), investigating the impact of various factors on the sweep coefficients, gravity segregation degree, and miscible degree in the three CO_2 flooding patterns. These factors are discussed from three aspects: geology, oil viscosity, and injection–production parameters. Section 4.5 employs the out-of-bag permutation method within the Random Forest algorithm to identify the main controlling factors influencing the CO_2 sweep coefficients. Finally, our study concludes with a presentation of the findings in Section 5.

2. Materials and Methods

2.1. Materials

The crude oil and formation water used in the experiments were sampled from the Jilin oil field, and the crude oil fractions are shown in Table 1. CO_2 was purchased from the Beijing Analytical Instrument Factory, and the purity of the CO_2 was 99.95 mol%.

Table 1. Crude oil composition.

Comp.	mol. (%)	Comp.	mol. (%)	Comp.	mol. (%)	Comp.	mol. (%)
sCO_2	0.153	C7	3.835	C17	2.249	C27	1.062
N_2	2.818	C8	5.131	C18	1.999	C28	1.024
C1	16.193	C9	4.225	C19	1.921	C29	0.936
C2	3.938	C10	3.897	C20	1.764	C30	0.905
C3	3.224	C11	3.36	C21	1.604	C31	0.7
IC4	1.675	C12	3.256	C22	1.554	C32	0.716
NC4	2.978	C13	3.271	C23	1.431	C33	0.548
IC5	0.904	C14	2.697	C24	1.385	C34	0.532
NC5	2.594	C15	2.746	C25	1.232	C35	0.476
C6	2.431	C16	2.208	C26	1.153	C36+	5.275

2.2. Apparatus

The PVT analyzer (purchased from DBR, Edmonton, AB, Canada) had a maximum working pressure of 103 MPa and a full operating temperature of 180 °C. The flow chart of the PVT analyzer is shown in Figure 1. The slim tube experimental device was formed in the laboratory. The tube length was 16.0 m, the inner diameter was 6.35 mm, the outer diameter was 9.60 mm, the porosity was 33%, and the permeability of the gas measurement was 3.2 mD. The flow chart of the slim tube experiment is shown in Figure 2.

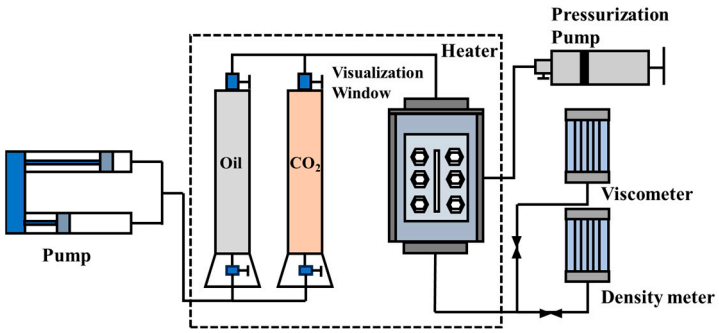


Figure 1. The diagram of the PVT analyzer.

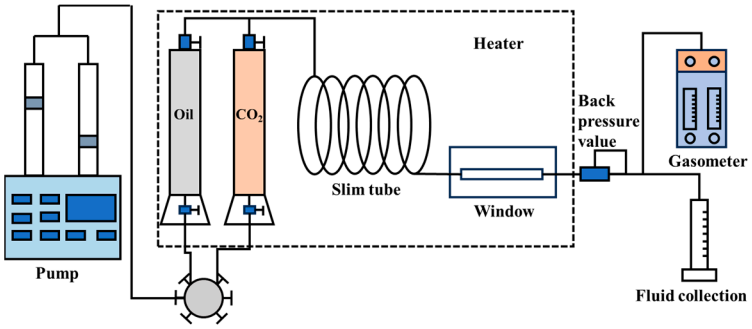


Figure 2. The diagram of the slim tube experiment.

2.3. Methods

2.3.1. PVT Experiments

1. Constant Composition Expansion experiments (CCE)

Constant composition expansion experiments were used to determine the relationship between the volume and pressure of crude oil with a constant mass at reservoir temperature to obtain parameters such as the saturation pressure, the compression coefficient, the relative volume, and the density of the formation fluids. The steps were as follows: the PVT analyzer was evacuated at a temperature of 97.3 °C, then a certain amount of crude oil was transferred to the PVT analyzer in a single phase at a constant temperature for more than 4 h, and the crude oil was pressurized to a pressure P_1, which was higher than the reservoir pressure. Above the saturation pressure, pressurization was carried out via stepwise depressurization at 1~2 MPa per step; below the saturation pressure, volume expansion was carried out at 1~20 cm^3 per step. After each depressurization step and expansion, the sample was stirred and stabilized thoroughly, and the pressure and volume were recorded. The experiment was stopped when the sample was expanded to twice the original sample.

2. Differential Liberation experiments (DL)

Differential liberation or multi-degassing experiments involved degassing crude oil at reservoir temperature in multi-graded pressure reductions to measure the relationship between oil and gas properties and composition with pressure. The crude oil was kept in a single phase, fully stirred to equilibrate, and then stabilized at saturation pressure. The sample was depressurized in three to five pressure steps, with each depressurization recording the sample volume and the volume of gas produced.

3. Swelling Tests (STs)

Swelling tests were used to measure the relationship between the density and viscosity of crude oil with the molar fraction of CO_2 by gradually increasing the molar fraction of the injected CO_2. First, the volume of the crude oil was tested at saturation pressure, and then a certain amount of CO_2 was injected into the crude oil at this pressure. The pressure increased until all the CO_2 was dissolved to test the saturation pressure, swelling factor, oil viscosity, and other parameters of the CO_2–crude oil system. The above experimental steps were repeated until the molar content of CO_2 in the system reached about 80%, which was when the experiment was stopped.

2.3.2. Slim Tube Experiments

The slim tube model was heated at the experimental temperature, and the slim tube was evacuated for more than 12 h. The pore volume was measured by injecting toluene into the tube model. The slim tube model was saturated with crude oil at the experimental pressure. CO_2 was injected at a constant rate of 15.00 cm^3/h to displace the crude oil. Whenever a certain amount of CO_2 was injected, the output oil and gas volumes, injection pressure, and back pressure were measured. Fluid phase and color changes were observed through

a high-pressure observation window. The experiment was stopped after injecting 1.2 times the pore volume of CO_2. The above experiments were repeated, and the experimental pressure was changed to determine the minimum miscible pressure for CO_2 flooding.

2.3.3. Testing the Relative Permeability Curves Based on Unsteady-State Method

1. Oil–water relative permeability curve

First, the absolute permeability ka of the core was measured. The core was then vacuumed to saturate the formation water, and the effective pore volume and porosity were measured. Under the back pressure of 24.5 MPa, the irreducible water saturation Swc was established by injecting formation oil to displace formation water at the injection rate of 0.2 mL/min, and the oil phase permeability under irreducible water saturation was measured. Keeping the same back pressure, the water flooding experiment was carried out at the injection rate of 0.2 mL/min. The data relating to the water breakthrough time, pressure difference, cumulative oil production, and cumulative liquid production were recorded. When the water cut at the core outlet reached 99.5%, the experiment was stopped. The relative permeabilities of the oil phase and water phase under different water saturations were measured, and the relative permeability curve was drawn.

2. Gas–oil relative permeability curve

The core was saturated with formation water, and the water phase permeability was measured. The formation oil was injected at an injection rate of 0.2 mL/min to displace the formation water until the water saturation reached irreducible water saturation. The oil phase permeability under irreducible water saturation was measured. CO_2 was injected to displace oil at an injection rate of 0.2 mL/min, and the displacement pressure, oil production, and gas production at each time were recorded. When only gas was produced at the outlet of the core, the experiment was stopped, the relative permeabilities of the oil phase and gas phase under different gas saturations were measured, and the gas–oil relative permeability curve was finally drawn.

3. Numerical Simulation

3.1. Simulation for Slim Tube Experiments and 1-D CO_2 Flooding

3.1.1. Simulation for Slim Tube Experiments

The 1-D numerical simulation model was based on the parameters of the slim tube experiment. The cumulative CO_2 injection volume was 1.2 PV. The fluid parameters simulated for the slim tube experiments were obtained based on the fitting results of CCE, DL, and ST experiments with the WinProp module of the CMG software. The parameters of the thin tube model are shown in Table 2.

Table 2. Slim tube model parameters.

Parameters	Values
Number of grids	50 × 1 × 1
Grid size	32 cm × 5.8 mm × 5.8 mm
Porosity/%	0.33
Permeability/mD	3.2
Injection pressure constraints/MPa	35.0
Gas injection rate/(PV/d)	0.1

3.1.2. Simulation for 1-D CO_2 Flooding

The GEM module of CMG software was used to establish a 1-D numerical simulation model of CO_2 flooding, the EOS of which was fitted by using the WinProp module of CMG software. The values of the model parameters (porosity, permeability, saturation, and so on) were consistent with those in the Jilin oil field, and the processes of miscible flooding, immiscible flooding, and partly miscible flooding were simulated by setting different original reservoir pressures. To ensure the accuracy of the solution, the model was

solved by using a fully implicit method. The relative permeability curves were obtained through the experiments, which are shown in Figure 3. The relative permeability of the oil, gas, and water phases was calculated using the Stone II method. The characterization of the miscible state was based on Coats' component model theory, which describes the miscible state through the relationship between the relative permeability and the interfacial tension of oil and gas. The reference interfacial tension $\sigma_{og}{}^{r}$ was set to 0.5 mN/m. When the interfacial tension σ_{og} was higher than 0.5 mN/m, the interfacial tension did not affect the relative permeability curves. When the interfacial tension σ_{og} was lower than 0.5 mN/m, oil started to be displaced in the form of miscible flooding. The relative permeability curve of miscible flooding was determined via interfacial tension interpolation. The interpolation equations are shown in Equations (1)–(3). The values of the 1-D model parameters are shown in Table 3.

$$k_{rom} = m \times k_{ro} + (1 - m) \times \frac{k_{row}(S_w) + k_{rg}(S_g)}{2} \times \frac{S_o}{(1 - S_w)} \quad (1)$$

$$k_{rgm} = m \times k_{rg} + (1 - m) \times \frac{(k_{row}(S_W) + k_{rg}(S_g)}{2} \times \frac{S_g}{(1 - S_w)} \quad (2)$$

$$m = \begin{cases} 1 & \sigma_{og} > \sigma_{og}^{r} \\ (\frac{\sigma_{og}}{\sigma_{og}^{r}})^{n} & \sigma_{og} \leq \sigma_{og}^{r} \end{cases} \quad (3)$$

where k_{rom} and k_{rgm} are the relative permeability of oil and gas after interpolation; k_{ro} and k_{rg} are the relative permeability of oil phase and gas before interpolation; and S_w, S_g, and S_o are the saturation of water, gas, and oil, respectively. k_{row} is the relative permeability of water in the oil–water relative permeability curve, which is a function of water saturation S_w; k_{rg} is the relative permeability of gas in the oil–gas relative permeability curve, which is a function of gas saturation, S_g; σ_{og} is the actual oil–gas interfacial tension in the model; $\sigma_{og}{}^{r}$ is the reference interfacial tension, which takes the value of 0.5 mN/m; and m is the interpolated value, the value of which depends on the relationship between σ_{og} and $\sigma_{og}{}^{r}$. n is the index of the ratio of actual oil–gas interfacial tension σ_{og} to the reference interfacial tension $\sigma_{og}{}^{r}$, which characterizes the transition speed of the relative permeability curve of immiscible flooding to miscible flooding.

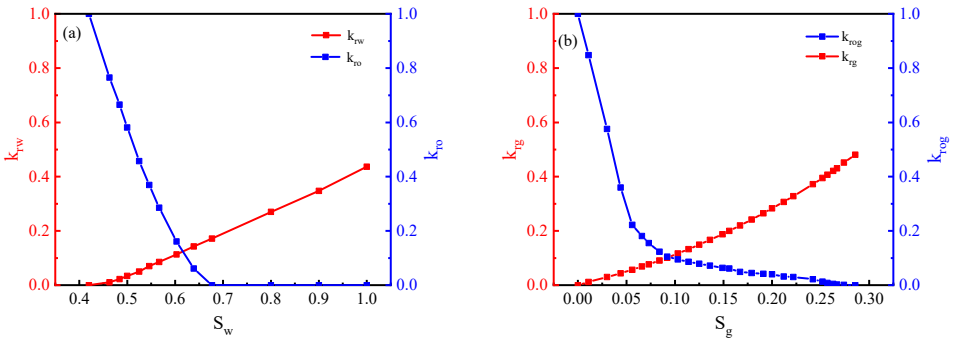


Figure 3. Relative permeability curve: (**a**) water/oil and (**b**) gas/oil.

3.2. Simulation for 2-D CO_2 Flooding with Quarter Five-Spot Well Pattern

A 2-D numerical simulation model of CO_2 flooding components was established using the GEM module of the CMG software, the EOS equations and relative permeability curves of which were consistent with the 1-D model. The model's porosity, permeability, and saturation were set with reference to the Jilin oil field. The miscible, immiscible, and partly miscible flooding processes were simulated by setting different original reservoir pressures. Continuous gas injection (CGI) was simulated with a constant gas injection period of 40 years. The model parameters are shown in Table 4.

Table 3. The 1-D numerical simulation parameters.

Parameters	Values
Number of grids	300 × 1 × 1
Grid size	1 m × 1 m × 1 m
Porosity/%	0.13
Temperature/°C	97.3
Permeability/mD	4.5
Initial formation pressure/MPa	16.0 (immiscible flooding) 22.0 (partly miscible flooding) 26.0 (miscible flooding)
Gas injection rate/(m^3/d)	0.00195 (reservoir condition)
Well bottom pressure constraint/Mpa	40.0 (upper limit) 10.0 (lower limit)

Table 4. The 2-D numerical simulation parameters.

Parameters	Values
Number of grids	25 × 25 × 5
Grid size	8 m × 8 m × 0.6 m
Porosity/%	0.13
Temperature/°C	97.3
Permeability/mD	4.5
Initial formation pressure/Mpa	16.0 (immiscible flooding) 22.0 (partly miscible flooding) 26.0 (miscible flooding)
Gas injection rate/(m^3/d)	0.77 (reservoir condition)
Well bottom pressure constraint/Mpa	40.0 (upper limit) 10.0 (lower limit)

Compared with the traditional numerical simulation model for CO_2 flooding, a series of improvements were made in this model: to enhance model convergence and solution accuracy, the model was solved using the fully implicit method instead of the traditional IMPSE method. In the iterative solution method, a nine-point difference format was used to suppress the grid orientation effect of CO_2 flooding instead of the conventional five-point difference format. For the general seepage equation $\Delta u = f$, the five-point differential and nine-point differential solution equations for the center point $u_{i,j}$ are shown in Equations (4) and (5), respectively. In Equations (4) and (5), f is a function of (x_i,y_j), which represents the external driving force or source term at positions(i,j) in the differential equation.

$$\frac{1}{h^2}(u_{i-1,j} - 2u_{i,j} + u_{i+1,j}) + \frac{1}{h^2}(u_{i,j-1} - 2u_{i,j} + u_{i,j+1}) = f_{ij} \quad (4)$$

$$\frac{1}{h^2}(u_{i-1,j+1} + u_{i+1,j+1} + u_{i-1,j-1} + u_{i+1,j-1} + 4(u_{i,j+1} + u_{i,j-1} + u_{i-1,j} + u_{i+1,j}) - 20u_{i,j}) = f_{ij} \quad (5)$$

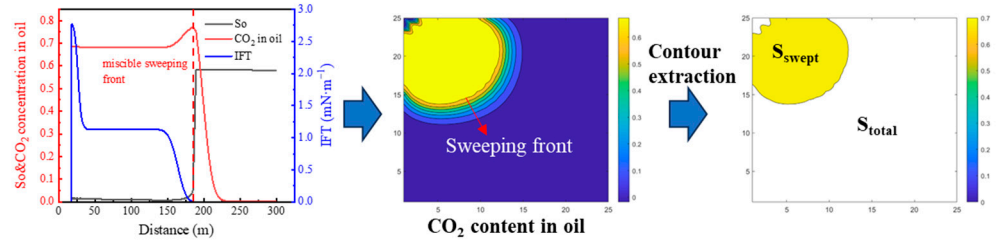
3.3. Solution of Sweep Coefficient for CO_2 Flooding

Parameters such as the CO_2 content in the oil and the interfacial tension of each grid obtained from the solution of the 2-D numerical model were imported into MATLAB R2022a by programming a data reading algorithm. The discrete grid data were expanded using linear or cubic interpolation methods. Contour maps of CO_2 content in oil and interfacial tension at different moments of CO_2 flooding were drawn. The contour lines corresponding to the miscible and immiscible front of CO_2 flooding were extracted. The polygon areas surrounded by the contour lines were solved, and the sweep coefficient at the

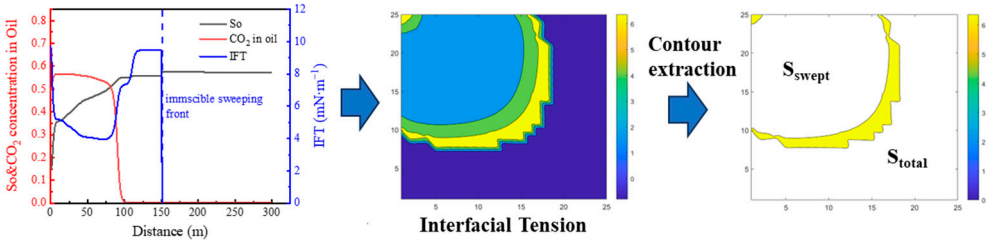
corresponding time could be obtained compared with the total grid area. The mechanism is shown in Figure 4, and the sweep coefficient E_{sweep} is calculated as shown in Equation (6).

$$E_{sweep} = \frac{S_{swept}}{S_{total}} \times 100\% \quad (6)$$

where S_{swept} and S_{total} are the areas enclosed by the contour line of the CO_2 front and the coordinate axis and the total grid area, respectively.



(**a**) Miscible flooding



(**b**) Immiscible flooding

Figure 4. Schematic diagram of sweep coefficient calculation.

3.4. Main Controlling Factor Assessment of CO_2 Flooding Based on Random Forest Algorithm

Different ranges of values were assigned to each parameter affecting the sweep coefficients of CO_2 flooding, and 1000 sets of numerical simulation models with different combinations of parameters were formed using the Latin hypercube design method, which can make the values of each parameter satisfy the normal distribution. The range of values for each parameter is shown in Table 5. The sweep coefficients of CO_2 flooding for different parameter combinations were obtained by solving the 1000 sets of models. The Bootstrap sampling method was used to form 800 training sets and 200 prediction sets. The 800 training sets were used to construct multiple decision trees to develop a Random Forest model. Predictions were made on the prediction sets, and the ballot method was used to decide the regression or classification results. Different numbers of decision trees and leaves were set to form different Random Forest models and solve the prediction errors (MSE) of the different Random Forest models. The numbers of decision trees and leaves with minimum MSE were preferred as the parameters of the optimal Random Forest model. The principle of the Random Forest algorithm is shown in Figure 5. Based on the out-of-bag data permutation method (OOB), the optimized Random Forest model was used to evaluate the importance of each influencing factor (FI). The main steps were as follows: (1) For decision tree i, the prediction error rate e_1 of out-of-bag data was calculated. (2) After randomly replacing the observations of the influencing factor X_j, the decision tree was constructed again, and the prediction error rate e_2 of the out-of-bag data was calculated. (3) The differences between the two error rates were calculated and standardized to calculate the average MDA_j in all decision trees, which was the factor importance value

(FI_j). The larger the FI_j value, the higher the importance of the parameter X_j. The calculation of FI_j is shown in Equation (7) [47].

$$FI_j = MDA_j = \frac{1}{T}\sum_{t}^{T}\left[\frac{1}{|D_t|}\left(\sum_{X_i^j \in D_t^j}\sum\left(R_k(X_i^j) - y_i^k\right)^2 - \sum_{X_i \in D_t}\sum_{k}\left(R_k(X_i) - y_i^k\right)^2\right)\right] \quad (7)$$

where T is the number of decision trees; (X_i, y_i) is the training set; X_i^j is the sample after a random exchange of the j-type influence parameter of X_i; D_t is the out-of-bag sample set of the decision tree $_t$, and D_t^j is the sample set formed after the j-th type of influence parameter exchange; and $R(X_i)$ is the predicted output of sample X_i. y_i^k is the regression output of the k-type influence parameter under multi-objective regression.

Table 5. Range of values for each parameter.

Parameters	Minimum Value	Maximum Value	Unit
Permeability	0.5	100	mD
Porosity	0.05	0.2	/
Reservoir thickness	3.0	30.0	m
Permeability ratio	1.1	100	/
Well spacing	50	300	M
Injection rate	0.1	2.0	m^2/d (RC)
Oil viscosity	0.74	33.52	mPa·s

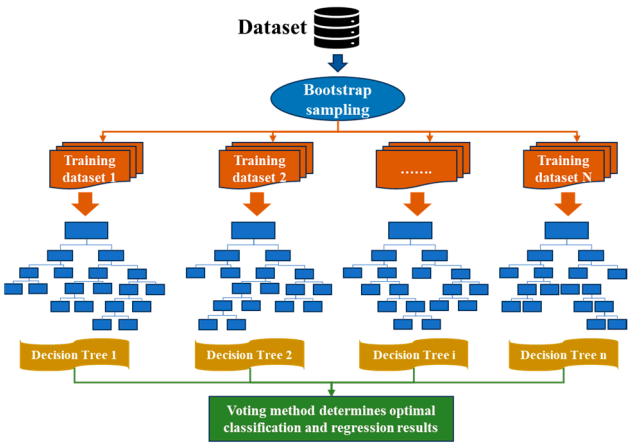


Figure 5. Schematic diagram of Random Forest algorithm.

4. Discussion

4.1. PVT Fitting and Establishment of EOS Equation for Reservoir Fluid

The saturation pressure P_{sat}, relative volume, oil phase density, viscosity, and swelling factor of reservoir fluid were measured by using CCE, DL, and ST experiments. The C_{17+} component of the formation oil was divided into three components, C_{17}–C_{26}, C_{27}–C_{39}, and C_{40+}, and the C_1–C_{16} components were merged into five components, C_1, C_2, C_3+C_4, C_5+C_6, and C_7–C_{16}. By adjusting the critical pressure P_c, critical temperature T_c, binary interaction coefficient, and other parameters of the heavy components, the fluid component model was obtained based on fitting the results of the PVT experiments. The results are shown in Figure 6. Some parameters of the EOS after PVT fitting are shown in Table 6. It can be seen from Figure 6 that the saturation pressure of the pure oil phase used in the experiment was 7.16 MPa, and the viscosity at saturation pressure was 1.74 mPa·s. When the mole fraction of injected CO_2 was 80%, the oil saturation pressure increased to 39.7 MPa, the viscosity decreased to 0.72 mPa·s, and the swelling factor increased to 1.8762. The swelling and viscosity reduction effects of CO_2 on crude oil were propitious to

enhancing oil recovery. The experimental results were compared with the fitting results. It could be seen that the above component, the splitting and merging scheme for oil phase components, could accurately fit the results of PVT experiments, and the obtained EOS parameters could better simulate the high-temperature and high-pressure physical properties of crude oil in reservoirs.

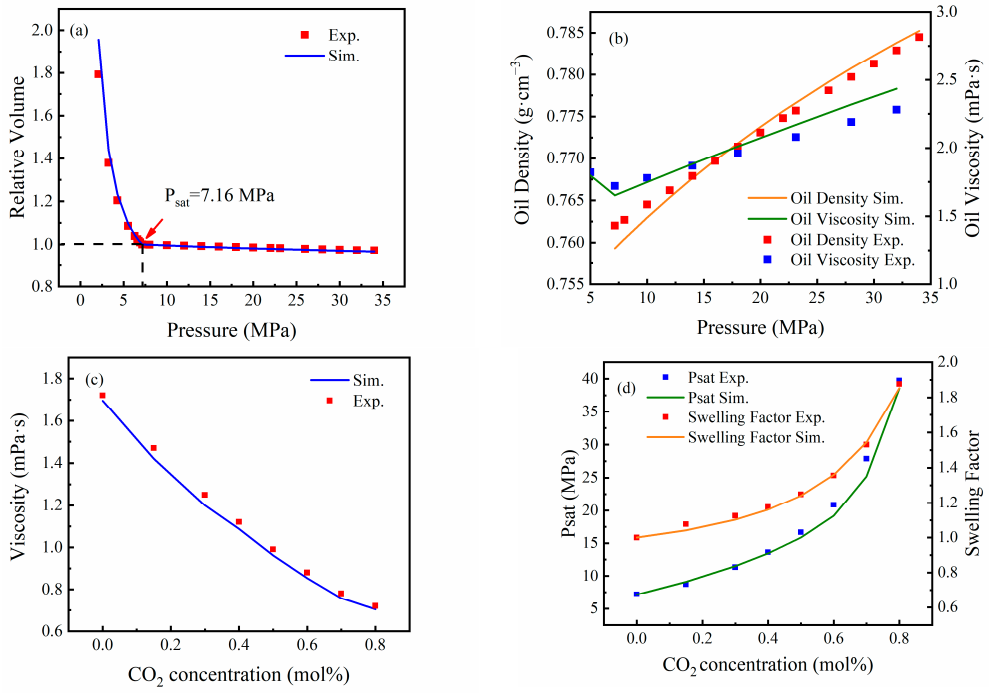


Figure 6. Results of PVT fitting: (**a**) relative volume fitting, (**b**) oil density and oil viscosity fitting, (**c**) swelling test fitting, and (**d**) saturation pressure and swelling factor fitting.

Table 6. Parameters of EOS after PVT fitting.

Components	mol. (%)	P_c (atm)	T_c (K)	M_w (g/mol)	V_c (m^3/kmol)
CO_2	0.153	72.80	304.20	44.01	0.0940
N_2	2.818	33.50	126.20	27.99	0.0898
C_1	16.193	45.40	190.60	16.05	0.0990
C_2	3.938	48.20	305.40	30.09	0.1480
C_3+C_4	7.877	39.02	406.11	52.38	0.2371
C_5+C_6	5.929	31.51	486.50	76.99	0.3335
C_7-C_{16}	31.58	19.82	624.24	148.05	0.5701
C_{17}-C_{26}	15.87	13.63	653.87	289.86	1.2768
C_{27}-C_{39}	9.478	11.76	878.05	444.69	1.8926
C_{40+}	6.164	10.60	989.31	716.21	3.2964

4.2. Determination of Minimum Miscible Pressure Based on Slim Tube Experiment Simulation

The CO_2 displacement experiment was carried out with a slim tube model at the formation temperature of 97.3 °C, and the displacement pressure ranged from 18 MPa to 30 MPa. The cumulative amount of injected CO_2 was 1.2 PV. The recovery factors of CO_2 flooding under different displacement pressures were calculated, and the results are shown in Figure 7a. When the displacement pressure was less than 22.10 MPa, the recovery factor of CO_2 flooding was low, which was an immiscible displacement process, and the recovery factor increased rapidly with the increase in displacement pressure. When the displacement pressure increased from 18 MPa to 23.11 MPa, the recovery degree rose from 76.89% to 94.53%. When the displacement pressure was higher than 22.10 MPa, the CO_2 flooding pattern turned to miscible flooding, and the increase in the recovery factor slowed

down. When the displacement pressure increased from 23.11 MPa to 30.0 MPa, the recovery degree only increased from 94.53% to 96.08%. The sections of immiscible and miscible displacement were fitted, and the displacement pressure corresponding to the intersection of the fitting lines was 22.10 MPa. Based on the EOS equation formed in Section 4.1, a 1-D slim tube numerical model was established to simulate the results of the tube experiment. The results are shown in Figure 7b. The maximum fitting error of the recovery factor under immiscible flooding was about 7%, and the maximum fitting error of the recovery degree under miscible flooding was about 0.8%. The simulation results showed that the minimum miscible pressure was 23.30 MPa, and the error compared with the experimental results was 5.4%, which indicated that the EOS equation formed by PVT fitting could accurately reflect the characteristics of crude oil and could be used for subsequent numerical simulation work.

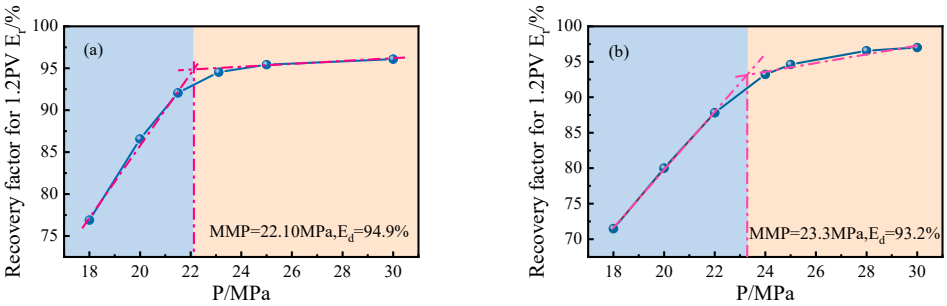


Figure 7. Results of slim tube experiment and slim tube experimental simulation: (**a**) slim tube experiment and (**b**) slim tube experimental simulation.

4.3. Front Movement Rules of CO_2 Flooding under Different Flooding Patterns

Currently, the classification of CO_2 flooding is mainly based on the relationship between original reservoir pressure and minimum miscible pressure, which is divided into miscible flooding, immiscible flooding, and near-miscible flooding. However, in the oil field development process, the reservoir pressure field undergoes dynamic changes due to the conduction between the injection and production wells, changing the miscible degree. Therefore, according to the miscible degree, CO_2 flooding was divided into three displacement patterns: (1) In miscible flooding (MF), the pressure between the injection and production wells was higher than the minimum miscible pressure, and the miscible degree was 1.0. (2) In partly miscible flooding (PMF), the original formation pressure of the reservoir was lower than the minimum miscible pressure, but the pressure near the injection well was higher than the minimum miscible pressure due to the reservoir energy enhancement of gas injection, thus forming a miscible flooding zone. The oil production of production wells decreased the reservoir pressure, and the immiscible flooding zone was formed within a certain range near the production well. The miscible degree of partly miscible flooding was between 0 and 1.0. (3) In immiscible flooding (IMF), the pressure between injection and production wells after gas injection was lower than the minimum miscible pressure, and the displacement process maintained immiscible flooding. The miscible degree of immiscible flooding was 0. By establishing a 1-D numerical simulation model, the distribution of CO_2 composition in the oil phase, oil saturation, and oil–gas interfacial tension between the injection and production wells under different displacement patterns of CO_2 flooding was studied, and the miscible/immiscible front position and front movement rules were determined. The results are shown in Figure 8. Figure 8a also shows the distribution of fluid properties between the injection and production wells in relation to miscible flooding. The oil saturation of miscible flooding maintained a meager value with increasing distance. Then, it increased rapidly to the initial oil saturation S_{oi}, showing the characteristics of a piston-like displacement. The interfacial tension increased rapidly with distance and then gradually decreased to the platform value. When the distance reached a certain value, it gradually decreased to 0. The CO_2 content in the oil phase increased

rapidly and reached the platform value. The CO_2 content then increased gradually to the maximum value after increasing a certain distance and finally decreased to the original CO_2 content in the oil phase. According to the distribution of the above three parameters, the inter-well phase zone of miscible flooding was divided into a pure gas zone, a two-phase zone, a miscible zone, a diffusion zone, and an unswept zone. The gas zone was near the gas injection well area, where the oil saturation and interfacial tension were zero due to continuous CO_2 injection and miscibility. In the two-phase zone, the light components gradually evaporated into the gas phase, forming a rich gas that migrated to the production wells, significantly increasing the content of heavy components in crude oil at the miscible rare edge, thus forming an oil–gas two-phase zone. The crude oil in this zone was mainly residual oil with a high heavy component content. Due to the subsequent injection and dissolution of CO_2, the CO_2 content in this zone was significantly higher than the initial level. In the miscible zone, the rich gas in the miscible front contacted the crude oil through the condensate miscible effect, so the light component and CO_2 content in the oil phase increased significantly. The difference in the component content between oil and gas decreased, and the interfacial tension, therefore, gradually decreased and finally reached zero interfacial tension. The oil saturation suddenly changed to the initial oil saturation in this zone. In the diffusion zone, CO_2 entered the crude oil mainly through diffusion. As the distance increased, the diffusion effect gradually weakened, and the CO_2 content decreased to the initial level. The unswept zone only contained the pure oil phase. The interfacial tension was zero, the oil saturation was equal to the initial oil saturation, and the CO_2 content in the oil phase was equal to the initial value. The above analysis shows that the front of the miscible zone should be located at the maximum CO_2 content in the oil phase. Figure 8b shows the distribution of fluid properties between the injection and production wells in the case of immiscible flooding. With the increased distance, the oil saturation of immiscible flooding increased slowly to the initial oil saturation, forming a wide range of two-phase zones. The interfacial tension decreased rapidly with increasing distance, then increased sharply after a certain distance, and finally decreased to zero. The content of CO_2 in the oil phase decreased slightly at first and then decreased significantly to the initial level after a certain distance. Similarly, the injection–production inter-well phase zone of immiscible flooding was divided into two-phase, diffusion, and unswept zones. In the two-phase zone, due to the dissolution of CO_2 in the oil phase, the interfacial tension was reduced to 4 mN/m, and the CO_2 content in the oil phase was increased to about 0.55, which was lower than the CO_2 content in the case of miscible flooding. In the diffusion zone, the interfacial tension increased gradually due to the formation of a CO_2 concentration diffusion gradient. The interfacial tension reached the maximum at the junction of the diffusion zone and the unswept zone, defined as the immiscible front of immiscible flooding. Figure 8c shows the distribution of the fluid properties between injection and production wells in partly miscible flooding. The oil saturation of partly miscible flooding first maintained a meager value (residual oil saturation) with increasing distance. It then gradually increased to the initial oil saturation S_{oi}, but the increase amplitude was less than that of miscible flooding. The interfacial tension had two extreme values with the increase in distance. The CO_2 content in the oil phase gradually increased from the platform value of about 0.63 to the maximum value of 0.75. It then gradually decreased to the original CO_2 content in the oil phase. Unlike miscible and immiscible flooding, partly miscible flooding had both miscible and immiscible zones. In the miscible zone, due to condensate miscibility, the CO_2 content in the oil phase reached the maximum value, and the interfacial tension was reduced to zero, reaching the miscible state. In the immiscible zone, as the distance increased, the pressure between the injection and production wells decreased to less than the minimum miscible pressure, and the CO_2 in the oil phase re-evaporated into the gas phase, resulting in the gradual decrease in the CO_2 content in the oil phase and the rapid increase in interfacial tension. The displacement process changed from miscible flooding to immiscible flooding. The inter-well fluid zone divisions of the three displacement patterns are summarized in Figure 9. In addition, the gas injection volume was fixed at 0.3 HCPV, and the front

movement positions of miscible flooding, partly miscible flooding, and immiscible flooding were compared, as shown in Figure 7d. The front movement of immiscible flooding was the fastest to reach the production well. The front of the immiscible zone in partly miscible flooding was located at 170 m, and the front of the miscible zone was located at 134 m, which indicated that the front movement velocity of the immiscible zone in partly miscible flooding was faster than that of the miscible zone. Therefore, immiscible flooding was more likely to cause gas channeling problems than miscible and partly miscible flooding.

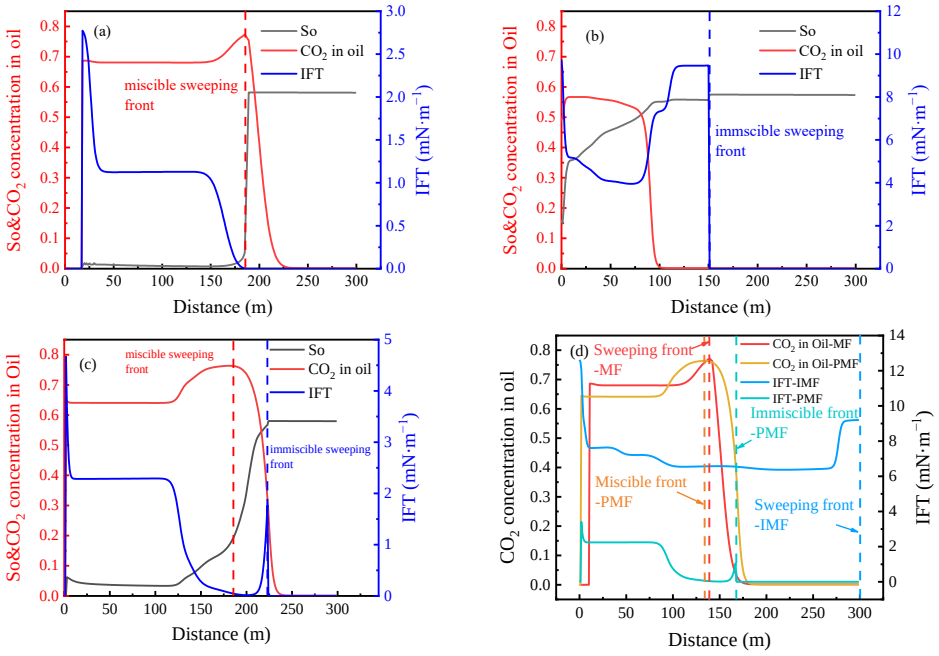


Figure 8. Distribution of fluid properties between wells: (**a**) miscible flooding (MF), (**b**) immiscible flooding (IMF), (**c**) partly miscible flooding (PMF), and (**d**) comparison chart (0.3 HCPV).

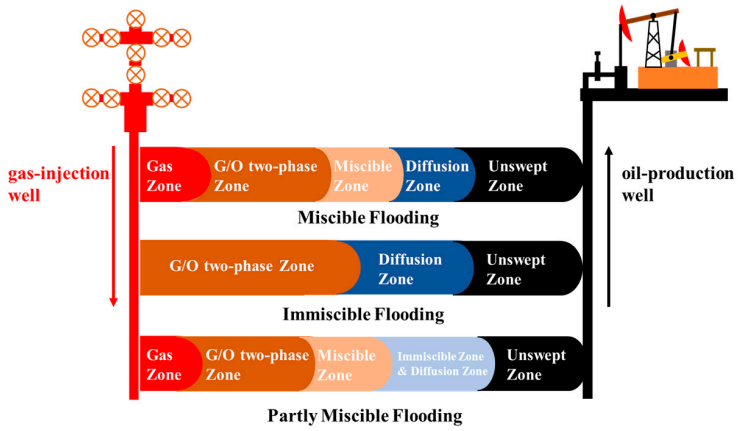


Figure 9. Division of inter-well fluid phase zones for three CO_2 displacement patterns.

4.4. Front Movement Rules of CO_2 Flooding under Different Flooding Patterns

According to the fluid phase zone division results of miscible, immiscible, and partly miscible flooding proposed in Section 4.3, the reservoir numerical simulation models of three displacement patterns were established based on the quarter five-point well pattern. The distribution of oil–gas interfacial tension and CO_2 content in the oil phase under different displacement patterns were output by MATLAB, and the contour map was formed. The effective sweep coefficient of CO_2 under different displacement patterns was solved by the program. In addition, the ratio of the maximum sweep coefficient E_{smax} to the

minimum sweep coefficient E_{smin} between layers was defined as the gravity overlap degree (GSD), as shown in Equation (8), to characterize the strength of the gravity overlap during CO_2 flooding. The larger the GSD value was, the stronger the gravity overlap effect of the displacement process was. The ratio of the miscible zone swept volume $V_{s\text{-}mis}$ to the total swept volume $V_{s\text{-}total}$ of partly miscible flooding was defined as the miscible degree (D_m), as shown in Equation (9), to characterize the strength of the miscible degree in the process of partly miscible flooding. The larger the D_m, the stronger the influence of miscibility on the sweep coefficient in the partly miscible flooding, and the range of the miscible degree D_m was 0~1.0. The effects of different factors on the sweep coefficient of CO_2 under three displacement patterns were studied from geological parameters, crude oil viscosity, and injection–production parameters.

$$GSD = \frac{E_{smax}}{E_{smin}} \tag{8}$$

$$D_m = \frac{V_{s\text{-}mis}}{V_{s\text{-}total}} \tag{9}$$

4.4.1. Geological Parameters

1. Permeability

The relationships between permeability and sweep coefficients of miscible flooding, partly miscible flooding, and immiscible flooding are compared in Figure 10a. The sweep coefficients of CO_2 under the three flooding patterns increased first and then decreased with increased permeability. However, the sweep coefficient of miscible flooding was higher than that of partly miscible and immiscible flooding. When the permeability was low, the sweep coefficients of the three displacement patterns were low due to the high seepage resistance in the reservoir, which was the main controlling factor affecting the sweep coefficient. When the permeability increased to 2 mD, the sweep coefficient gradually increased due to decreased seepage resistance. The sweep coefficient of miscible flooding reached 74.46%, while those of the partly miscible and immiscible flooding were 73.50% and 63.62%, respectively. When the permeability further increased, the sweep coefficients of the three displacement patterns gradually decreased. This was because the viscosity and density of CO_2 were lower than that of crude oil, and it was easy to produce gravity overlap in the reservoir with low seepage resistance, move to the top of the reservoir, and produce the crude oil in the top layer. The gravity segregation degrees (GSD values) of the three displacement patterns were analyzed, and the results are shown in Figure 10a. The GSD values of the three displacement patterns increased with increased permeability. When the permeability reached 100 mD, the GSD values of miscible, immiscible, and partly miscible flooding were 12.47, 69.44, and 51.75, respectively. The gravity segregation degree of miscible flooding was the lowest, followed by partly miscible flooding, and immiscible flooding was the highest. This was because the miscible effect continuously enriched CO_2 in the displacement process, and its density and viscosity were gradually similar to those of crude oil, so gravity segregation was significantly weakened. Figure 10b shows the variation in the sweep coefficient and miscible degree of partly miscible flooding with permeability. When the permeability was 0.5 mD, due to the large seepage resistance and high gas injection pressure, the overall pressure of the reservoir was increased so that CO_2 displaced crude oil in the form of miscible flooding, and the miscible degree (D_m value) was 1.0. With the increase in permeability, the seepage resistance decreased, and CO_2 flooding began to show the characteristics of partly miscible flooding, where both miscible and immiscible zones could be observed. When the permeability increased to 20 mD, the D_m value decreased to 0.52. This was mainly because the increase in permeability led to enhanced overlap, and CO_2 easily channeled along the top of the reservoir, resulting in a continuous decrease in the formation pressure, thus reducing the miscible degree. When the permeability increased to 100 mD, the miscibility rose to 0.70. The increased permeability reduced the seepage resistance, and the migration velocity of the immiscible

front was accelerated. After gas channeling, the sweeping volume of the immiscible zone decreased due to the weak ability of the immiscible zone to sweep oil in both sides of the main streamline, while the miscible front continued to move and displace the oil on both sides, thus increasing the miscible degree.

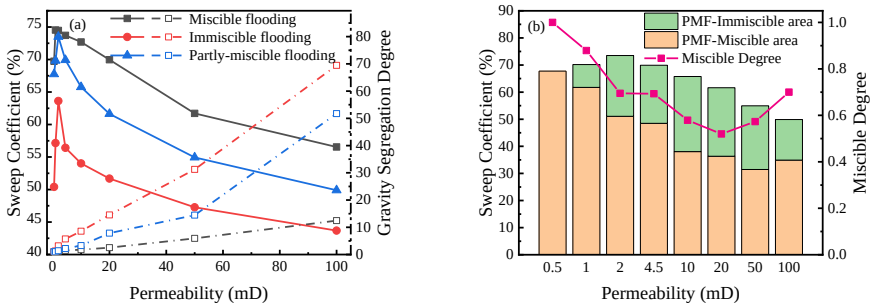


Figure 10. Relationship between permeability and sweep coefficient. (**a**) Comparison chart. (**b**) Sweep coefficient and miscible degree of partly miscible flooding (PMF).

2. Porosity

The relationships between the porosity and the sweep coefficient under three displacement patterns were compared, and the results are shown in Figure 11a. With the increase in porosity, the sweep coefficients of the three displacement patterns decreased gradually, and the sweep coefficients of miscible flooding and partly miscible flooding were higher than those of immiscible flooding. When the porosity was 0.03, the sweep coefficients of miscible, immiscible, and partly miscible flooding were 97.70%, 86.20%, and 92.13%, respectively. When the porosity increased to 0.3, the sweep coefficients of the three displacement patterns decreased to 50.46%, 42.98%, and 49.15%. The porosity affected the sweep coefficient, which was mainly attributed to the gravity segregation degree. It can be seen from Figure 10a that the GSD values of the three displacement patterns increased with the increase in porosity, and the GSD value of immiscible flooding was always greater than those of miscible flooding and partly miscible flooding. When the porosity was 0.3, the GSD value of immiscible flooding was 8.97, while the GSD values of miscible and partly miscible flooding were 1.93 and 13.57, respectively. The sweep coefficient and miscible degree of partly miscible flooding were analyzed, and the results are shown in Figure 11b. With the increase in porosity, the sweep coefficient of the immiscible zone of partly miscible flooding decreased significantly, but the sweep coefficient of the miscible zone increased slightly and then decreased slowly, and the sweep coefficient of the miscible zone decreased from 43.52% to 35.58%. The miscible degree rose from 0.47 to 0.72. On one hand, the increase in porosity accelerated the movement of the immiscible front and miscible front to production wells, but the moving velocity of the miscible front was slower. On the other hand, it was beneficial to the multi-contact miscibility in the movement of the miscible front, thus enhancing the miscible degree.

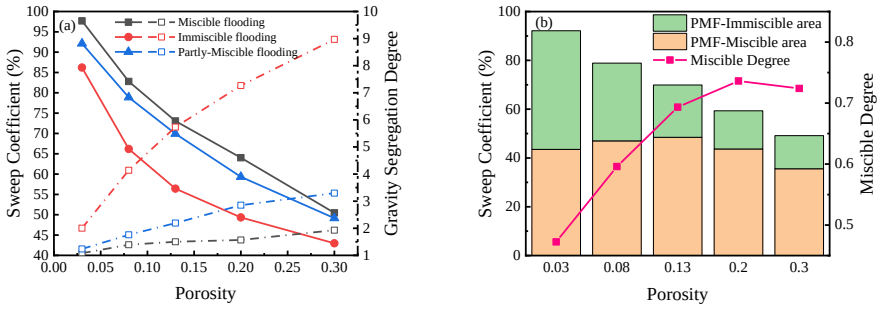


Figure 11. Relationship between porosity and sweep coefficient. (**a**) Comparison chart. (**b**) Sweep coefficient and miscible degree of partly miscible flooding (PMF).

3. Reservoir thickness

The influence of the reservoir thickness on CO_2 sweep coefficients of miscible flooding, partly miscible flooding, and immiscible flooding was studied by changing the reservoir thickness from 1.5 m to 10.0 m. The results are shown in Figure 12a. The sweep coefficients of CO_2 in the three displacement patterns decreased with the increase in reservoir thickness. When the reservoir thickness was 1.5 m, the sweep coefficients of miscible, partly miscible, and immiscible flooding were 86.85%, 82.75%, and 79.65%, respectively. When the reservoir thickness increased to 10.0 m, the sweep coefficients of the three displacement patterns decreased to 36.19%, 34.18%, and 33.01%, respectively. In addition, the GSD values of the three displacement patterns were 1.1~1.3, with a reservoir thickness of 1.5 m. When the reservoir thickness increased to 10.0 m, the GSD values of miscible flooding, partly miscible flooding, and immiscible flooding increased to 8.4, 16.4, and 78.1, respectively. The reservoir thickness had the most significant influence on immiscible flooding. Therefore, the variation in the gravity segregation degree caused by the change in the reservoir thickness was the critical factor affecting the sweep coefficient. The sweep coefficient and miscible degree of partly miscible flooding were analyzed, and the results are shown in Figure 12b. With the increase in the reservoir thickness, the sweep coefficients of miscible and immiscible zones of partly miscible flooding decreased gradually, but the miscible degree increased slightly from 0.62 to 0.74. This was mainly because the effect of the gravity segregation degree on the immiscible zone was stronger than that on the miscible zone. The increase in the reservoir thickness made the immiscible and miscible fronts move to the production well on the horizon and expand vertically simultaneously. The movement of the immiscible front was faster than that of the miscible front, so the immiscible zone quickly broke through to the production well in the high part of the reservoir. The sweeping of the miscible zone was more uniform, which ultimately improved the miscible degree.

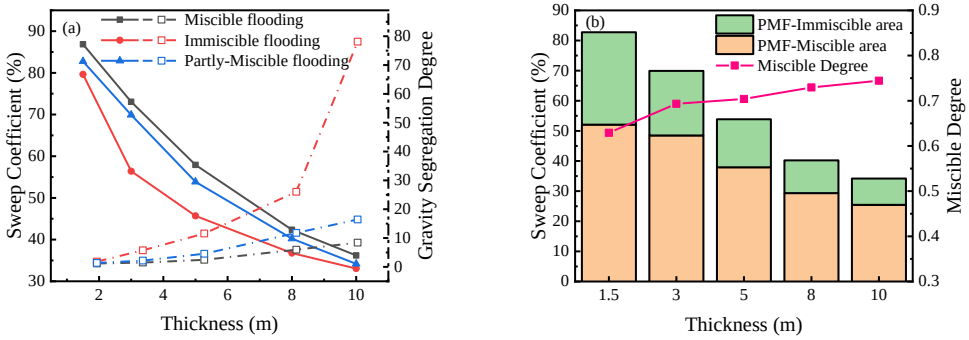


Figure 12. Relationship between thickness and sweep coefficient. (**a**) Comparison chart. (**b**) Sweep coefficient and miscible degree of partly miscible flooding (PMF).

4. Permeability Ratio

Two-layer heterogeneous models were established to study the influence of the permeability ratio on the sweep coefficients. The permeabilities of different layers changed in an anti-rhythmic pattern, the ratio of which ranged from 2 to 100. The results are shown in Figure 13a,b. The sweep coefficients of the whole layers and low-permeable zone decreased significantly under the three displacement patterns with the increased permeability ratio. When the permeability ratio was 10, the sweep coefficient of immiscible flooding was only 0.89%. In comparison, the sweep coefficients of miscible and partial miscible flooding were 4.8% and 2.8%, respectively, which were both lower than 5%. The result indicated the influence of heterogeneity on miscible flooding, and partly miscible flooding was weaker than immiscible flooding. Under different displacement patterns, the upper limit of the anti-rhythm reservoir permeability ratio suitable for applying CO_2 flooding was about 5.0.

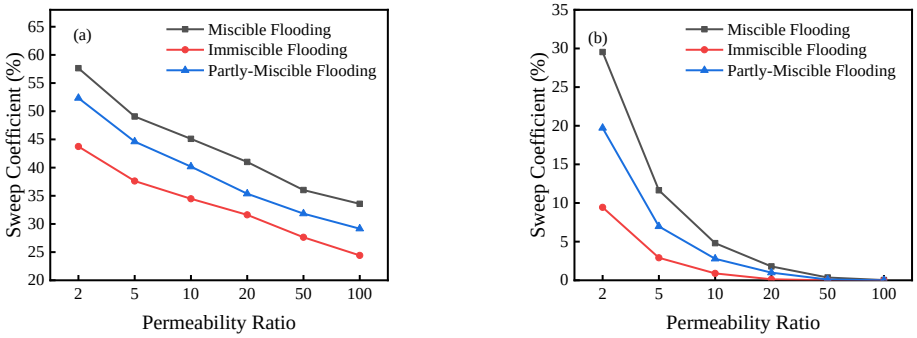


Figure 13. Relationship between permeability and sweep coefficient. (**a**) Total sweep coefficient and (**b**) sweep coefficient of low-permeable zone.

4.4.2. Injection–Production Parameters

1. Well spacing

The influence of injection–production well spacing on the CO_2 sweep coefficients of miscible flooding, partly miscible flooding, and immiscible flooding was studied in relation to a well spacing variation range of 100~300 m. The results are shown in Figure 14a. The sweep coefficients in the three displacement patterns decreased with the increase in well spacing. The increase in well spacing delayed the movement velocity of miscible and immiscible fronts to the production well in the horizontal direction. It significantly enhanced the gravity overlap of CO_2 in the vertical direction, so the sweep coefficients were reduced considerably. However, the reduced sweep coefficients of miscible and partly miscible flooding were mainly dominated by the weakening of the front movement velocity in the horizontal direction, and the gravity segregation degree did not change. When the well spacing increased to 300 m, the GSD values of miscible and partly miscible flooding increased from 1.0 and 1.2 to 2.1 and 3.6, respectively. The decrease in the sweep coefficient of immiscible flooding was mainly affected by gravity overlap, and the GSD value increased from 1.8 to 11.0. Figure 14b shows the influence of well spacing on the sweep coefficient and miscible degree of partly miscible flooding. Although the increase in well spacing reduced the total sweep coefficient of partly miscible flooding, the sweep coefficient of the miscible zone increased first and then decreased, and the miscible degree rose from 0.44 to 0.74. This was attributed to the delay in the miscible front moving through the production well. The effect of miscible flooding could be exploited adequately. When the well spacing was further increased, the gravity overlap of the miscible front was gradually enhanced, moving to the top of the reservoir and breaking through to the production well so that crude oil at the bottom of the reservoir could not be effectively displaced. When the well spacing was 200 m, it could not only ensure a higher sweep coefficient and miscible degree but also maximize the sweep coefficient of the miscible zone, giving full play to the role of miscible flooding.

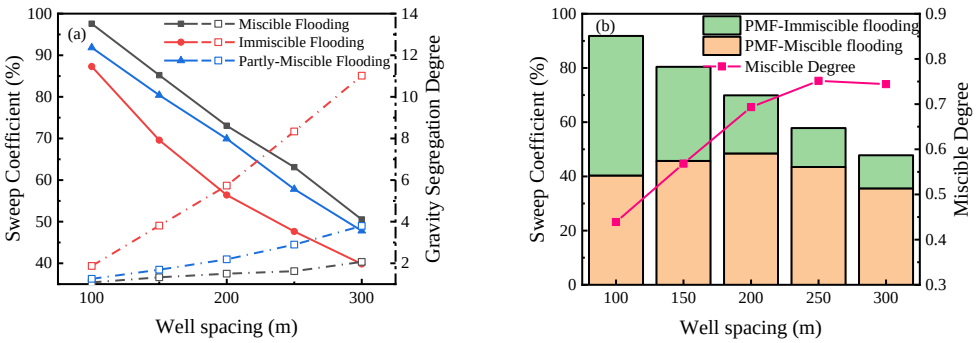


Figure 14. Relationship between well distance and sweep coefficient. (**a**) Comparison chart. (**b**) Sweep coefficient and miscible degree of partly miscible flooding (PMF).

2. Gas injection rate

The influence of the gas injection rate on the sweep coefficients of the three CO_2 flooding patterns was studied with the gas injection rate variation range of 85.98~517.5 m^3/d. The results are shown in Figure 15a. The sweep coefficients of CO_2 in the three CO_2 flooding patterns increased significantly first and then decreased slightly with an increasing gas injection rate. When the gas injection rate reached 517.5 m^3/d, the sweep coefficients of the three were about 70%. The GSD values of the three displacement patterns were significantly weakened with the increase in the gas injection rate. When the gas injection rate increased to 517.5 m^3/d, the GSD values of the three displacement patterns were about 1.01–1.07, which could achieve uniform displacement in each layer. The gas injection rate had two effects on the increasing CO_2 sweep coefficient. On one hand, the higher gas injection rate was beneficial to recovering reservoir energy, increasing the formation pressure to above the minimum miscible pressure, which made partly miscible flooding and immiscible flooding transition to miscible flooding. On the other hand, it promoted the seepage velocity of the miscible and immiscible fronts in the horizontal direction and inhibited vertical movement. However, the overhigh gas injection rate will accelerate gas channeling in the production wells. Hence, the sweep coefficients of the three displacement patterns decreased slightly with an increasing gas injection rate. Figure 15b shows the influence of the gas injection rate on the sweep coefficient and miscible degree of partly miscible flooding. When the gas injection rate was lower than 170.81 m^3/d, the sweep coefficient of the miscible zone and miscible degree were almost zero. When the gas injection rate exceeded 261.61 m^3/d, the sweep coefficient of the miscible zone reached 70%, and the miscible degree increased from 0.69 to 1.0. The miscible degree and sweep coefficient could be enhanced by appropriately increasing the gas injection rate for partly miscible and immiscible flooding.

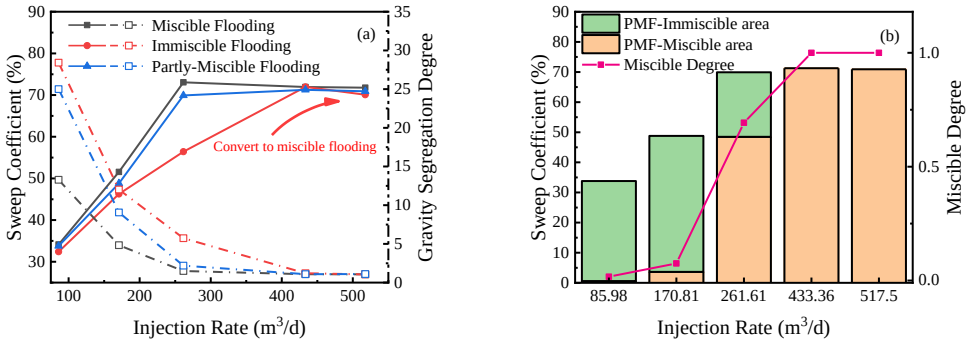


Figure 15. Relationship between injecting rate and sweep coefficients. (**a**) Comparison chart. (**b**) Sweep coefficient and miscible degree of partly miscible flooding (PMF).

4.4.3. Crude Oil Viscosity

The influence of the crude oil viscosity on the sweep coefficients of the three CO_2 flooding patterns was studied in relation to a gas injection rate variation range of 0.74~12.18 mPa·s. The results are shown in Figure 16a. The sweep coefficients of miscible and partly miscible flooding decreased with the increase in crude oil viscosity. When the viscosity of crude oil increased to 12.18 mPa·s, the sweep coefficients of miscible flooding and partly miscible flooding decreased from 80.42% and 78.98% to 64.42% and 49.92%, respectively. However, the gravity segregation degrees of miscible and partly miscible flooding remained almost unchanged with increasing crude oil viscosity, which were 1.40 and 1.60, respectively. Therefore, the decreases in the sweep coefficients of miscible flooding and partly miscible flooding were mainly due to the high seepage resistance caused by the increase in crude oil viscosity, and the influence of gravity overlap on the sweep coefficient was relatively small. The sweep coefficient of immiscible flooding decreased first and then increased with the increase in crude oil viscosity, and the GSD value rose first and then decreased. When the viscosity of crude oil was 4.98 mPa·s, the sweep coefficient of immiscible flooding reached the minimum value of 53%, and the GSD value increased to 5.27. When the viscosity of crude oil rose

to 12.18 mPa·s, the sweep coefficient of immiscible flooding increased to 61.89%, and the GSD value decreased to 2.05. The change of the sweep coefficient of immiscible flooding had an excellent corresponding relationship with the variation in the gravity segregation degree. The influence of crude oil viscosity on the sweep coefficient and miscible degree of partly miscible flooding is shown in Figure 16b. The miscible degree of partly miscible flooding decreased first and then increased with the increase in crude oil viscosity and finally dropped from 0.78 to 0.71. When the viscosity of crude oil increased by 12.18 mPa·s, the sweep coefficient of the miscible zone decreased from 61.34% to 44.45%. In contrast, the sweep coefficient of the immiscible zone first increased to 22.59% and then dropped to 17.76%. The increase in crude oil viscosity made the multi-contact miscibility between CO_2 and crude oil more difficult, decreasing the sweep coefficient of the miscible zone. In addition, increased crude oil viscosity inhibited the horizontal movement of the immiscible zone and intensified the vertical overlap, thus decreasing the miscible degree. However, the overhigh viscosity of crude oil strengthened the horizontal viscous fingering, making the immiscible zone break through the production well more easily along the horizontal direction.

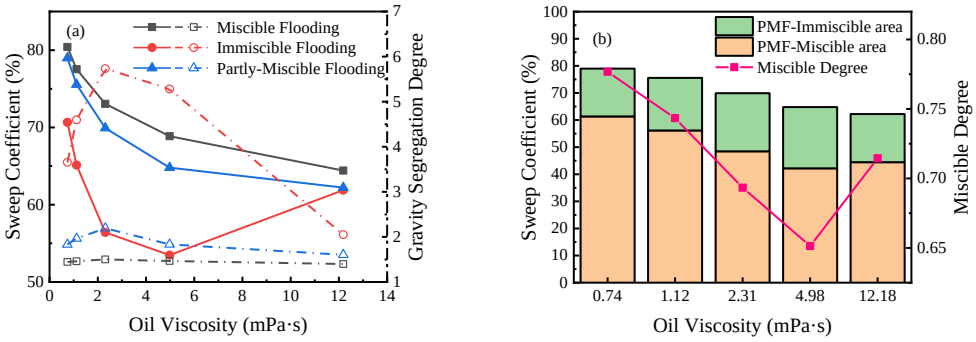
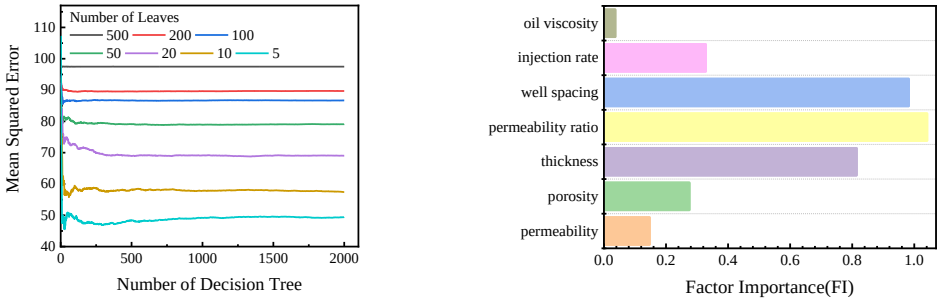


Figure 16. Relationship between oil viscosity and sweep coefficient. (**a**) Comparison chart. (**b**) Sweep coefficients and miscible degree of partly miscible flooding (PMF).

4.5. Analysis of the Main Controlling Factors of CO_2 Flooding Sweep Coefficient Based on the Random Forest Algorithm

Based on the single-factor analysis of the CO_2 flooding sweep coefficient in Section 4.4, the parameter variation ranges of different influencing factors were set, and 1000 sets of CO_2 flooding numerical simulation models were formed by using a Latin hypercube design. The Bootstrap sampling method was used to create 800 training sets and 200 testing sets. The Random Forest model was established by constructing multiple decision trees using the 800 training sets. The testing sets were predicted, and the voting method determined the prediction results. The number of decision trees and the number of leaves in the Random Forest model were optimized to obtain the optimal model parameters. The optimized Random Forest model was used to calculate the decrease rate MDA of the prediction accuracy before and after the permutation of the out-of-bag data of a certain influencing factor (such as porosity, permeability, etc.), which was used as a parameter to evaluate the importance degree (FI) of the influencing factor. The larger the FI value, the greater the influence of the factors on the sweep coefficient. The parameter optimization results of Random Forest are shown in Figure 17a. Under the condition of the same number of leaves, the mean square error MSE of the prediction results decreased rapidly with the increase in the number of decision trees. However, when the number of decision trees increased to 500, MSE almost did not change. Increasing the number of decision trees will lead to overfitting the model, so the optimal number of decision trees was 500. In addition, under the same number of decision trees, MSE increased with the increase in the number of leaves. Thereby, the optimal number of leaf nodes was five. The importance degree of the influencing factors of the CO_2 flooding sweep coefficient is shown in Figure 17b. The factors affecting the sweep coefficient of CO_2 flooding were ranked in order of importance degree (FI) as follows: permeability ratio, well spacing, reservoir thickness, gas injection rate, porosity, permeability, and

crude oil viscosity. The main controlling factor affecting the sweep coefficients of CO_2 flooding was the permeability ratio, the importance degree (FI) of which reached 1.04. In the field application of CO_2 flooding, attention should be paid to the problem that the low-permeability layer caused by the high-permeability ratio cannot be effectively utilized and the gravity overlap problem of CO_2 flooding in thick reservoirs.



(**a**) Optimization of Random Forest parameters (**b**) Factor importance of CO_2 flooding (FI)

Figure 17. Analysis results of main controlling factors of CO_2 flooding sweep coefficient.

5. Conclusions

Based on the fitting results of the PVT and slim tube experiments in the Jilin oil field, the 1-D and 2-D reservoir numerical simulation models of CO_2 flooding were developed to analyze the movement rules relating to the CO_2 front in miscible, partly miscible, and immiscible flooding, along with the influence of different factors on the sweep coefficient. The main controlling factors affecting the sweep coefficient of CO_2 flooding were determined using the out-of-bag data permutation method based on the Random Forest algorithm.

(1) The miscible front was located at the point of maximum CO_2 content in the oil phase, and the immiscible front was located at the point of maximum interfacial tension near the production well. The movement speed of the immiscible front was faster than that of the miscible front, so gas channeling was more likely to occur in immiscible flooding. Comparatively, miscible and partly miscible flooding yielded higher sweep coefficients than immiscible flooding, underscoring the advantageous effect of miscibility in achieving uniform CO_2 sweeping within the reservoir.

(2) Regarding geological factors, the increases in porosity, permeability, and reservoir thickness intensified the gravity overlap effect and reduced the sweep coefficients of CO_2 under the three displacement patterns. The increase in the permeability ratio also notably reduced the sweep coefficient, albeit to a lesser extent, in miscible and partly miscible flooding when compared with immiscible flooding. The upper limit of the reservoir permeability ratio suitable for applying CO_2 flooding under different displacement patterns was about 5. Concerning the injection–production parameters, the increase in well spacing amplified the seepage resistance in the horizontal direction, leading to reduced sweep coefficients in the cases of miscible and partly miscible flooding. In immiscible flooding, the reduction in the sweep coefficients was predominantly attributed to gravity overlap. Elevating the gas injection rate enhanced the miscibility degree in partly miscible flooding and immiscible flooding while inhabiting the gravity overlap, thus enhancing the sweep coefficient of CO_2 flooding. Crude oil viscosity primarily governed the sweep coefficients in miscible and partly miscible flooding by elevating the seepage resistance, whereas in immiscible flooding, gravity overlap took precedence in determining the sweep coefficient.

(3) The main controlling factor affecting the sweep coefficient of CO_2 flooding was the permeability difference, and the factor importance FI reached 1.04. In the field application of CO_2 flooding, attention should be paid to the problem of ineffective displacement in low-permeable zones in heterogeneous reservoirs.

Author Contributions: Conceptualization, X.Q. and T.Z.; methodology, X.Q.; software, X.Q.; validation, W.L., Y.S. and M.D.; formal analysis, W.L.; investigation, Z.L.; resources, X.Q.; data curation, X.Q. and M.W.; writing—original draft preparation, X.Q.; writing—review and editing, W.L.; visualization, D.H.; supervision, D.H.; project administration, D.H.; funding acquisition, W.L. All authors have read and agreed to the published version of the manuscript.

Funding: This research was funded by PetroChina's major scientific and technological project "Research and demonstration of key technologies for large-scale carbon dioxide capture, flooding and storage in the whole industrial chain", subject 03 "Study on CCUS geological fine description for oil displacement and key technologies in reservoir engineering" (2021ZZ01-03).

Data Availability Statement: The raw/processed data required to reproduce these findings cannot be shared at this time as the data also form part of an ongoing study.

Acknowledgments: The authors are grateful for the financial support of the CNPC in China.

Conflicts of Interest: Author Dongbo He was employed by the company JiDong Oilfield of PetroChina. The remaining authors declare that the research was conducted in the absence of any commercial or financial relationship that could be construed as a potential conflict of interest.

References

1. McLaughlin, H.; Littlefield, A.A.; Menefee, M.; Kinzer, A.; Hull, T.; Sovacool, B.K.; Bazilian, M.D.; Kim, J.; Griffiths, S. Carbon capture utilization and storage in review: Sociotechnical implications for a carbon reliant world. *Renew. Sustain. Energy Rev.* **2023**, *177*, 113215. [CrossRef]
2. Kumar, N.; Augusto Sampaio, M.; Ojha, K.; Hoteit, H.; Mandal, A. Fundamental aspects, mechanisms and emerging possibilities of CO_2 miscible flooding in enhanced oil recovery: A review. *Fuel* **2022**, *330*, 125633. [CrossRef]
3. Zhao, C.; Ju, S.; Xue, Y.; Ren, T.; Ji, Y.; Chen, X. China's energy transitions for carbon neutrality: Challenges and opportunities. *Carbon Neutrality* **2022**, *1*, 7. [CrossRef]
4. Zhao, K.; Jia, C.; Li, Z.; Du, X.; Wang, Y.; Li, J.; Yao, Z.; Yao, J. Recent Advances and Future Perspectives in Carbon Capture, Transportation, Utilization, and Storage (CCTUS) Technologies: A Comprehensive Review. *Fuel* **2023**, *351*, 128913. [CrossRef]
5. Yuan, S.; Ma, D.; Li, J.; Zhou, T.; Ji, Z.; Han, H. Progress and prospects of carbon dioxide capture, EOR-utilization and storage industrialization. *Pet. Explor. Dev.* **2022**, *49*, 955–962. [CrossRef]
6. Yue, P.; Zhang, R.; Sheng, J.J.; Yu, G.; Liu, F. Study on the Influential Factors of CO_2 Storage in Low Permeability Reservoir. *Energies* **2022**, *15*, 344. [CrossRef]
7. Tsopela, A.; Bere, A.; Dutko, M.; Kato, J.; Niranjan, S.C.; Jennette, B.G.; Hsu, S.Y.; Dasari, G.R. CO_2 injection and storage in porous rocks: Coupled geomechanical yielding below failure threshold and permeability evolution. *Pet. Geosci.* **2022**, *28*, 1. [CrossRef]
8. Haeri, F.; Myshakin, E.M.; Sanguinito, S.; Moore, J.; Crandall, D.; Gorecki, C.D.; Goodman, A.L. Simulated CO_2 storage efficiency factors for saline formations of various lithologies and depositional environments using new experimental relative permeability data. *Int. J. Greenh. Gas Control* **2022**, *119*, 103720. [CrossRef]
9. Wei, J.; Zhou, X.; Zhou, J.; Li, J.; Wang, A. Experimental and simulation investigations of carbon storage associated with CO_2 EOR in low-permeability reservoir. *Int. J. Greenh. Gas Control* **2021**, *104*, 103203. [CrossRef]
10. Li, L.; Su, Y.; Sheng, J.J.; Hao, Y.; Wang, W.; Lv, Y.; Zhao, Q.; Wang, H. Experimental and Numerical Study on CO_2 Sweep Volume during CO_2 Huff-n-Puff EOR Process in Shale Oil Reservoirs. *Energy Fuels* **2019**, *33*, 4017–4032. [CrossRef]
11. Wang, X.; Gu, Y. Oil Recovery and Permeability Reduction of a Tight Sandstone Reservoir in Immiscible and Miscible CO_2 Flooding Processes. *Ind. Eng. Chem. Res.* **2011**, *50*, 2388–2399. [CrossRef]
12. Bikkina, P.; Wan, J.; Kim, Y.; Kneafsey, T.J.; Tokunaga, T.K. Influence of wettability and permeability heterogeneity on miscible CO_2 flooding efficiency. *Fuel* **2016**, *166*, 219–226. [CrossRef]
13. Zargar, G.; Bagheripour, P.; Asoodeh, M.; Gholami, A. Oil-CO_2 minimum miscible pressure (MMP) determination using a stimulated smart approach. *Can. J. Chem. Eng.* **2015**, *93*, 1730–1735. [CrossRef]
14. Han, L.; Gu, Y. Optimization of Miscible CO_2 Water-Alternating-Gas Injection in the Bakken Formation. *Energy Fuels* **2014**, *28*, 6811–6819. [CrossRef]
15. Li, L.; Zhou, X.; Su, Y.; Xiao, P.; Chen, Z.; Zheng, J. Influence of Heterogeneity and Fracture Conductivity on Supercritical CO_2 Miscible Flooding Enhancing Oil Recovery and Gas Channeling in Tight Oil Reservoirs. *Energy Fuels* **2022**, *104*, 103203. [CrossRef]
16. Guo, Y.; Liu, F.; Qiu, J.; Xu, Z.; Bao, B. Microscopic transport and phase behaviors of CO_2 injection in heterogeneous formations using microfluidics. *Energy* **2022**, *256*, 124524. [CrossRef]
17. Alhosani, A.; Lin, Q.; Scanziani, A.; Andrews, E.; Blunt, M.J. Pore-scale characterization of carbon dioxide storage at immiscible and near-miscible conditions in altered-wettability reservoir rocks. *Int. J. Greenh. Gas Control* **2021**, *105*, 103232. [CrossRef]
18. Seyyedi, M.; Sohrabi, M. Assessing the Feasibility of Improving the Performance of CO_2 and CO_2-WAG Injection Scenarios by CWI. *Ind. Eng. Chem. Res.* **2018**, *57*, 11617–11624. [CrossRef]

19. Liu, Y.; Rui, Z. A Storage-Driven CO_2 EOR for a Net-Zero Emission Target. *Engineering* **2022**, *18*, 79–87. [CrossRef]
20. Al-Bayati, D.; Saeedi, A.; Myers, M.; White, C.; Xie, Q.; Clennell, B. Insight investigation of miscible $SCCO_2$ Water Alternating Gas (WAG) injection performance in heterogeneous sandstone reservoirs. *J. CO2 Util.* **2018**, *28*, 255–263. [CrossRef]
21. Ren, B.; Littlefield, J.; Jia, C.; Duncan, I. Impact of Pressure-Dependent Interfacial Tension and Contact Angle on Capillary Trapping and Storage of CO_2 in Saline Aquifers. In Proceedings of the SPE Annual Technical Conference and Exhibition, San Antonio, TX, USA, 2–7 October 2023.
22. Song, X.; Wang, F.; Ma, D.; Gao, M.; Zhang, Y. Progress and prospect of carbon dioxide capture, utilization and storage in CNPC oilfields. *Pet. Explor. Dev.* **2023**, *50*, 229–244. [CrossRef]
23. Kalteyer, J. A Case Study of SACROC CO_2 Flooding in Marginal Pay Regions: Improving Asset Performance. In Proceedings of the SPE Improved Oil Recovery Conference, Virtual, 31 August–4 September 2020.
24. Zhao, X.; Liao, X. Evaluation Method of CO_2 Sequestration and Enhanced Oil Recovery in an Oil Reservoir, as Applied to the Changqing Oilfields, China. *Energy Fuels* **2012**, *26*, 5350–5354. [CrossRef]
25. Chen, X.; Li, Y.; Tang, X.; Qi, H.; Sun, X.; Luo, J. Effect of gravity segregation on CO_2 flooding under various pressure conditions: Application to CO_2 sequestration and oil production. *Energy* **2021**, *226*, 120294. [CrossRef]
26. Al Hinai, N.M.; Saeedi, A.; Wood, C.D.; Myers, M.; Valdez, R.; Sooud, A.K.; Sari, A. Experimental Evaluations of Polymeric Solubility and Thickeners for Supercritical CO_2 at High Temperatures for Enhanced Oil Recovery. *Energy Fuels* **2018**, *32*, 1600–1611. [CrossRef]
27. Sun, X.; Long, Y.; Bai, B.; Wei, M.; Suresh, S. Evaluation and Plugging Performance of Carbon Dioxide-Resistant Particle Gels for Conformance Control. *SPE J.* **2020**, *25*, 1745–1760. [CrossRef]
28. Li, Z.; Su, Y.; Li, L.; Hao, Y.; Wang, W.; Meng, Y.; Zhao, A. Evaluation of CO_2 storage of water alternating gas flooding using experimental and numerical simulation methods. *Fuel* **2022**, *311*, 122489. [CrossRef]
29. Alsumaiti, A.M.; Hashmet, M.R.; Alameri, W.S.; Antodarkwah, E. Laboratory Study of CO_2 Foam Flooding in High Temperature, High Salinity Carbonate Reservoirs Using Co-injection Technique. *Energy Fuels* **2018**, *32*, 1416–1422. [CrossRef]
30. Song, Y.; Yang, W.; Wang, D.; Yang, M.; Jiang, L.; Liu, Y.; Zhao, Y.; Dou, B.; Wang, Z. Magnetic resonance imaging analysis on the in-situ mixing zone of CO_2 miscible displacement flows in porous media. *J. Appl. Phys.* **2014**, *115*, 401–410. [CrossRef]
31. Wang, H.; Tian, L.; Chai, X.; Wang, J.; Zhang, K. Effect of pore structure on recovery of CO_2 miscible flooding efficiency in low permeability reservoirs. *J. Pet. Sci. Eng.* **2021**, *208*, 109305. [CrossRef]
32. Chen, M.; Cheng, L.; Cao, R.; Lyu, C.; Rao, X. Carbon dioxide transport in radial miscible flooding in consideration of rate-controlled adsorption. *Arab. J. Geosci.* **2020**, *13*, 1–11. [CrossRef]
33. Coats, K.H.; Smith, B.D. Dead-End Pore Volume and Dispersion in Porous Media. *Soc. Pet. Eng. J.* **1964**, *4*, 73–84. [CrossRef]
34. Brattekås, B.; Haugen, M. Explicit tracking of CO_2-flow at the core scale using micro-Positron Emission Tomography (μPET). *J. Nat. Gas Sci. Eng.* **2020**, *77*, 103268. [CrossRef]
35. Wang, S.; Jiang, L.; Cheng, Z.; Liu, Y.; Song, Y. Experimental study on the CO_2-decane displacement front behavior in high permeability sand evaluated by magnetic resonance imaging. *Energy* **2021**, *217*, 119433. [CrossRef]
36. Duraid, A.B.; Ali, S.; Quan, X.; Myers, M.B.; Cameron, W. Influence of Permeability Heterogeneity on Miscible CO_2 Flooding Efficiency in Sandstone Reservoirs: An Experimental Investigation. *Transp. Porous Media* **2018**, *125*, 341–356. [CrossRef]
37. Lewis, E.; Dao, E.; Mohanty, K.K. Sweep Efficiency of Miscible Floods in a High-Pressure Quarter Five-Spot Model. *SPE J.* **2006**, *13*, 432–439. [CrossRef]
38. Hao, Y.; Li, J.; Kong, C.; Guo, Y.; Lv, G.; Chen, Z.; Wei, X. Migration behavior of CO_2-crude oil miscible zone. *Pet. Sci. Technol.* **2021**, *39*, 959–971. [CrossRef]
39. Li, J.; Cui, C.; Wu, Z.; Wang, Z.; Wang, Z.; Yang, H. Study on the migration law of CO_2 miscible flooding front and the quantitative identification and characterization of gas channeling. *J. Pet. Sci. Eng.* **2022**, *218*, 110970. [CrossRef]
40. Li, N.; Tian, J.; Ren, Z. The research on spread rule of CO_2 miscible region in low permeability reservoir. *Well Test.* **2014**, *23*, 2023101670. [CrossRef]
41. Al-Abri, A.; Sidiq, H.; Amin, R. Mobility ratio, relative permeability and sweep efficiency of supercritical CO_2 and methane injection to enhance natural gas and condensate recovery: Coreflooding experimentation. *J. Nat. Gas Sci. Eng.* **2012**, *9*, 166–171. [CrossRef]
42. Perrin, J.C.; Benson, S. An Experimental Study on the Influence of Sub-Core Scale Heterogeneities on CO_2 Distribution in Reservoir Rocks. *Transp. Porous Media* **2010**, *82*, 93–109. [CrossRef]
43. Lu, Y.; Liu, R.; Wang, K.; Tang, Y.; Cao, Y. A study on the fuzzy evaluation system of carbon dioxide flooding technology. *Energy Sci. Eng.* **2021**, *9*, 239–255. [CrossRef]
44. Bai, S.; Song, K.P.; Yang, E.L. Optimization of water alternating gas injection parameters of CO_2 flooding based on orthogonal experimental design. *Spec. Oil Gas Reserv.* **2011**, *20*, 48–52. [CrossRef]
45. Chenglong, L. Gas Channeling Influencing Factors and Patterns of CO_2-flooding in Ultra-Low Permeability Oil Reservoir. *Spec. Oil Gas Reserv.* **2018**, *25*, 82–86. [CrossRef]

46. Cui, C.; Yan, D.; Yao, T.; Wang, J.; Zhang, C.; Wu, Z. Prediction method of migration law and gas channeling time of CO_2 flooding front: A case study of Gao 89-1 Block in Shengli Oilfield. *Reserv. Eval. Dev.* **2022**, *12*, 741–747+763. [CrossRef]
47. Sinha, U.; Dindoruk, B.; Soliman, M.Y. Prediction of CO_2 Minimum Miscibility Pressure MMP Using Machine Learning Techniques. In Proceedings of the SPE-Improved Oil Recovery Conference, Virtual, 31 August–4 September 2020.

Disclaimer/Publisher's Note: The statements, opinions and data contained in all publications are solely those of the individual author(s) and contributor(s) and not of MDPI and/or the editor(s). MDPI and/or the editor(s) disclaim responsibility for any injury to people or property resulting from any ideas, methods, instructions or products referred to in the content.